

1 **FMRP BRIDGES R-LOOPS AND DHX9 THROUGH DIRECT**  
2 **INTERACTIONS**

3  
4  
5 Arijita Chakraborty<sup>1,#</sup>, Arijit Dutta<sup>2,#</sup>, Leonardo G. Dettori<sup>1</sup>, Leticia Gonzalez<sup>3</sup>, Xiaoyu Xue<sup>3</sup>,  
6 Heidi Hehny<sup>4</sup>, Patrick Sung<sup>2</sup>, Alaji Bah<sup>1</sup>, and Wenyi Feng<sup>1,\*</sup>

7  
8  
9 <sup>1</sup>Department of Biochemistry and Molecular Biology, SUNY Upstate Medical University, 750 East  
10 Adams Street, Syracuse, NY 13210, USA

11  
12 <sup>2</sup>Department of Biochemistry and Structural Biology, University of Texas Health San Antonio , 7703  
13 Floyd Curl Drive, San Antonio, TX 78229, USA

14  
15 <sup>3</sup>Department of Chemistry and Biochemistry, Texas State University, 601 University Dr.  
16 San Marcos, TX 78666

17  
18 <sup>4</sup>Department of Biology, Syracuse University, Syracuse, NY 13210, USA

19  
20 # These authors contributed equally to this work.

21 \* To whom correspondence should be addressed. Email: [fengw@upstate.edu](mailto:fengw@upstate.edu).

22

23 **ABSTRACT**

24 Fragile X Syndrome (FXS) occurs when mutations in the *FMR1* gene cause the absence or  
25 dysfunction of FMRP, known mainly as a translation repressor. We recently showed that FXS  
26 cells suffer genome-wide DNA double-strand breaks near R-loops under replication stress. The  
27 expression of FMRP, and not an FMRP-I304N mutant of the K-homology 2 RNA-binding  
28 domain, suppresses the R-loop-induced DNA breakage. These observations led us to  
29 hypothesize that FMRP safeguards the genome through promotion of R-loop detection and/or  
30 resolution. Here, we demonstrate that FMRP directly binds R-loops through multivalent  
31 interactions between the carboxy-terminal intrinsically disordered region and the R-loop sub-  
32 structures. We also show that the amino-terminal folded domain of FMRP directly binds DHX9,  
33 an R-loop resolvase, in a KH2-dependent manner. The FMRP-DHX9 interaction is recapitulated  
34 by co-immunoprecipitation in human cells. Our findings are consistent with a model in which  
35 FMRP recruits DHX9 to R-loop forming sites by bridging their interaction through its amino-  
36 and carboxy-termini, respectively.

37

38

39

40

## 41 INTRODUCTION

42 Fragile X syndrome (FXS) is a neurodevelopmental disorder due to epigenetic silencing or  
43 loss-of-function mutations of the *FMR1* gene encoding FMRP (Ciaccio et al., 2017; Sitzmann et  
44 al., 2018). FMRP is a nuclear-cytoplasmic RNA binding protein that regulates multiple  
45 biological processes of its diverse mRNA substrates, including their maturation in the nucleus,  
46 nuclear export, cytoplasmic transport, and ultimately, their translation at the synapse (Banerjee et  
47 al., 2018; Sudhakaran et al., 2014; Zhou et al., 2017).

48 Additionally, studies have suggested that FMRP is also involved in genome maintenance,  
49 though its exact role in the nucleus is not clear (Dockendorff and Labrador, 2019). We recently  
50 demonstrated that FXS patient-derived cells accumulate genome-wide DNA double strand  
51 breaks (DSBs), particularly during replication stress (Chakraborty et al., 2020). We further  
52 demonstrated that the DSBs in FXS cells were associated with R-loops, which are three-stranded  
53 nucleic acid structures formed during transcription when the nascent RNA stably anneals to the  
54 template DNA strand, displacing the non-template DNA strand. Finally, we showed that  
55 expression of FMRP, but not the FMRP-I304N mutant, ameliorated the R-loop-induced DSBs.  
56 Thus, our work suggested a genome protective role of FMRP by preventing R-loop accumulation  
57 during replication-transcription conflict.

58 The ability of FMRP to participate in multiple processes in the cell is attributed to the  
59 presence of multiple domains and their relative 3D-organization. All FMRP splice variants  
60 contain two amino (N-)terminal methylated lysine-binding Agenet domains (Age1 and Age2),  
61 three K-homology (KH0, KH1, and KH2) RNA binding domains and a carboxy (C-)terminal  
62 intrinsically disordered region (C-IDR), which in the case of the predominant isoform 1, contains  
63 an RNA binding RGG-box. Additionally, the presence of a nuclear localization signal and a  
64 nuclear export signal allows FMRP to shuttle between the nucleus and the cytoplasm, with  
65 approximately 4% of FMRP detected in the nucleus (Feng et al., 1997b).

66 In this study, we investigated how FMRP promotes R-loop resolution by testing if FMRP  
67 directly interacts with R-loops and R-loop resolvases. We purified recombinant FMRP and  
68 measured its capacity to bind various nucleic acid structures by electrophoretic mobility shift  
69 (EMSA) assay. We present evidence that FMRP interacts directly with R-loop structures  
70 specifically through its C-IDR. We also present evidence of FMRP interacting with known R-  
71 loop regulator proteins in vivo and in vitro, suggesting that FMRP might mediate the interaction  
72 between these proteins and R-loop structures. Our study represents a significant advance in the  
73 understanding of the mechanisms through which FMRP promotes genome integrity upon  
74 replication stress.

## 75 RESULTS

76 We previously showed that FXS patient-derived cells lacking FMRP have elevated  
77 genome-wide DSBs near R-loop forming sites when undergoing replication stress by aphidicolin  
78 (APH), a DNA polymerase inhibitor (Chakraborty et al., 2020). We proposed that FMRP  
79 protects the genome by preventing DSBs during induced replication-transcription conflict. Here  
80 we asked whether FMRP alters its expression level and/or its cellular localization in response to  
81 APH (Figure 1A). First, the total level of FMRP remained the same with and without APH  
82 (Figure 1-figure supplement 1A). However, the nuclear fraction of FMRP increased from 18%  
83 in DMSO (vehicle)-treated control cells to 24-36% in APH treatment (Figure 1B). In contrast,  
84 GAPDH (cytoplasmic) and Histone H3 (nuclear) controls maintained their respective subcellular  
85 localization, with or without APH (Figure 1B). We concluded that FMRP has substantial nuclear  
86 fraction in human lymphoblastoids, and it becomes further enriched in the nucleus in response to  
87 replication stress. Next, we wanted to visualize the localization of FMRP relative to R-loops.  
88 Immunofluorescence microscopy revealed a distinct staining pattern of FMRP, which was  
89 distributed in the cytoplasm and at the periphery of the nucleus (Figure 1C & Figure 1-figure  
90 supplement 1B-D) in untreated and DMSO-treated cells. Upon induction with APH, FMRP was  
91 enriched in the nucleus, particularly at 0.3  $\mu$ M APH, consistent with the chromatin fractionation  
92 experiments. RNA:DNA hybrid signals were also enhanced with APH, as we previously  
93 observed with fibroblasts derived from a FXS patient (Chakraborty et al., 2020). Notably,  
94 FMRP signals were closely associated with the RNA:DNA hybrid signals, suggesting a potential  
95 interaction between the protein and R-loops.

96 To test the ability of FMRP to directly bind R-loops, we resorted to recombinantly  
97 expressing and purifying full length FMRP, the N-terminal folded domain (N-Fold) and the C-  
98 terminal intrinsically disordered region (C-IDR) (Figure 2A and Figure 2-figure supplement  
99 1A&C). We then measured their binding affinities for R-loops with and without RNA overhangs  
100 and R-loop sub-structures including ssDNA, dsDNA, RNA, and DNA:RNA hybrid (Figure 2B)  
101 in an electrophoretic mobility shift assay (EMSA). DNA:RNA hybrids with or without a 5'  
102 DNA overhang produced nearly identical results for all proteins and therefore only DNA:RNA  
103 without overhang is shown. First, we observed binding between both the N-Fold and C-IDR of  
104 FMRP to the R-loop with 5' RNA overhang (Figure 2C&D) and the aforementioned sub-  
105 structures of R-loops with varying affinities (Figure 2-figure supplements 2&3). Due to the high  
106 propensity of FMRP to aggregate and precipitate at high concentrations (Sjekloca et al., 2009;  
107 Sjekloca et al., 2011), it was not feasible to obtain complete binding isotherms and determine the  
108 dissociation constants ( $K_D$ s) for some weak FMRP:substrate interactions (Figure 2-figure  
109 supplement 2). Of all the tested protein-nucleic acid pairs, the C-IDR and R-loop without  
110 overhang showed the highest affinity ( $K_D = 4.7 \pm 3.9$  nM, Figure 2E and Figure 2-figure  
111 supplement 2). Intriguingly, the interaction was weakened with a 5' RNA overhang to the R-  
112 loop ( $K_D = 149.1 \pm 9.9$  nM, Figure 2D). Moreover, while the C-IDR showed affinity towards  
113 ssDNA and dsDNA in isolation, it barely interacted with the DNA:RNA hybrid or ssRNA  
114 (Figure 2H and Figure 2-figure supplement 3). Therefore, we concluded that the C-IDR  
115 interacted with R-loops through simultaneous binding to the ssDNA and dsDNA or to the 3D  
116 architecture of the entire R-loop structure itself, with the RNA overhang interfering with the  
117 interaction. In contrast, the N-Fold bound R-loops with ssRNA overhang more tightly than those  
118 without overhang, albeit with still lower affinity than C-IDR (Figure 2F, Figure 2-figure  
119 supplements 2&3). Additionally, N-Fold showed affinities for ssRNA and ssDNA, but not



120 dsDNA nor the DNA:RNA hybrid (Figure 2F and Figure 2-figure supplements 2&3). Therefore,  
121 the N-Fold likely interacts with the R-loop through binding with the single stranded segments  
122 (RNA or DNA) of the R-loop. Consistent with this interpretation, while the full length FMRP  
123 (Figure 2-figure supplements 1D) binds R-loop without overhang with a lower affinity ( $K_D =$   
124  $288.7 \pm 4$  nM) compared to the C-IDR, it prefers the R-loop with RNA overhang (Figure 2I&J  
125 and Figure 2-figure supplements 2&3). We surmised that in the full length protein, the N-Fold  
126 interacted with the RNA overhang, thus minimizing the RNA's interference with C-IDR binding  
127 to the R-loop. Thus, our results demonstrated that the FMRP binding to R-loops involves  
128 multivalent interactions, with N-Fold and C-IDR showing varying affinities to all segments of an  
129 R-loop structure. Moreover, these multivalent interactions between FMRP and R-loops are  
130 modulated by intra- and inter-molecular cooperative and/or inhibitory effects within FMRP, as  
131 well as between FMRP and the R-loop sub-structures.

132 Next, we investigated the effect on R-loop binding by I304N, an FXS-causing mutant  
133 defective in RNA binding and polysome association (De Boulle et al., 1993; Feng et al., 1997a).  
134 We recently showed that FMRP-I304N had reduced ability to suppress R-loop-induced DSBs  
135 during programmed replication-transcription conflict (Chakraborty et al., 2020). We generated  
136 both the full length FMRP and N-Fold containing the I304N substitution (Figure 2A and Figure  
137 2-figure supplement 1B&D). While the mutation indeed disrupted the interactions between N-  
138 Fold with all substrates tested, it actually enhanced the binding of full length FMRP to R-loop  
139 with overhang (Figure 2C,G,I and Figure 2-figure supplements 2&3). These results suggested  
140 that although the I304N mutation may weaken the interaction between the N-Fold and substrates,  
141 it may also reduce the N-Fold's inhibitory effects on C-IDR binding to R-loops through a long-  
142 range intramolecular mechanism. Therefore, the inability of the FMRP-I304N mutant to  
143 suppress DSB formation may originate from downstream events (*e.g.*, recruitment of R-loop  
144 resolving factors) by the N-Fold, rather than from defective R-loop recognition *per se*, which  
145 mainly depends on C-IDR. Therefore, we next tested if FMRP interacts with known R-loop-  
146 interacting proteins.

147 To this date, we have observed interaction between FMRP and DHX9, a known R-loop  
148 helicase that has been shown to suppress R-loop formation and prevent chromosome breakage  
149 (Chakraborty and Grosse, 2011; Cristini et al., 2018). In an *in vitro* binding assay we observed  
150 that FMRP directly interacts with recombinantly expressed histidine tagged-DHX9 (Figure  
151 3A&B). Moreover, this interaction specifically occurred through the N-Fold domain (Figure  
152 3C). Interestingly, the mutant N-Fold-I304N failed to interact with DHX9 (Figure 3D),  
153 indicating that the KH2 domain, an integral part of the N-Fold domain organization, assists in the  
154 recruitment of R-loop resolving factors. Therefore, we hypothesized that FMRP bridges the  
155 interaction between R-loops and R-loop resolving factors, through its C-IDR and N-Fold,  
156 respectively. We next asked if FMRP interacts with DHX9 *in vivo*. Using the aforementioned  
157 GM06990 lymphoblastoids we first demonstrated co-immunoprecipitation of FMRP and its  
158 known interacting protein, FXR1 (FMR1 autosomal homolog 1), as a positive control (Zang et  
159 al., 2009) (Figure 3E). We also detected DHX9 interaction with FMRP through co-  
160 immunoprecipitation (Figure 3F). In addition, the complex pulled down by anti-DHX9 also  
161 comprised of Top III $\beta$  (Figure 3F), which has been recently implicated in the R-loop suppression  
162 by reducing negatively supercoiled DNA behind RNA polymerase II (Yang et al., 2014).

163

## 164 DISCUSSION

165 Our work directly builds on our previous report of a genome protective role of FMRP  
166 during replication stress-induced R-loop accumulation and DSBs (Chakraborty et al., 2020).  
167 Here we augmented this discovery by demonstrating direct interaction between FMRP and R-  
168 loops and DHX9. We provided, for the first time, direct evidence that the C-IDR can interact  
169 tightly with the R-loop structure. This is a remarkable finding, given that the same C-IDR also  
170 has the ability to interact with G-quadruplexes and SoSLIPs that both adopt very different 3D  
171 structures than R-loops (Bechara et al., 2009; Santoro et al., 2012; Vasilyev et al., 2015).  
172 Previous studies have demonstrated that the formation of R-loops and G-quadruplexes are  
173 potentially coupled during transcription (De Magis et al., 2019; Lee et al., 2020). Together with  
174 our finding, it appears that FMRP can bind both structures via its C-IDR, thus providing a  
175 mechanism for the functional linkage between these nucleic acid structures.

176 Based on the hierarchy of substrate binding by the FMRP segments we propose the  
177 following model (Figure 4). During replication-transcription conflict induced by APH treatment,  
178 FMRP binds to R-loops predominantly via its C-IDR, thereby allowing the KH domains to bind  
179 the trailing nascent ssRNA, and the N-terminal Agenet domains to presumably interact with  
180 methylated histone tails (not depicted) or R-loop resolving factors that contain motifs with  
181 methylated arginine or lysine residues. Here, we showed that FMRP interacts with one such R-  
182 loop resolving factors, DHX9, through its N-Fold domain. Moreover, the interaction is  
183 dependent on a bona-fide KH2 domain, suggesting that mutations in the KH domain may  
184 interfere with the Agenet domain's binding to other proteins through intra-molecular  
185 interactions. Overall, we propose that FMRP functions as a scaffold that bridges R-loops and R-  
186 loop resolving factors, such as DHX9 and Top III $\beta$ . A recent human interactome analysis in  
187 HeLa cells also revealed an interaction between FMRP and the THO-TREX complex, which  
188 functions at the interface of transcription elongation and mRNA export (Hein et al., 2015).  
189 THOC1, a subunit of the THO/TREX complex was present in the same complex as FMR1,  
190 DHX9 and other THOC proteins. Depletion of subunits in the hTHO complex causes DNA  
191 damage that is R-loop dependent (Dominguez-Sanchez et al., 2011). Our co-  
192 immunoprecipitation experiments also showed an interaction between FMRP and TopIII $\beta$ ,  
193 whose loss causes R-loop-mediated genome instability (Zhang et al., 2019). This result suggests  
194 that FMRP forms multiple docking sites for factors that resolve R-loops and ensures proper  
195 transcription, RNA processing and export.

196 Modular proteins such as FMRP and DHX9, which contain multiple folded domains  
197 interspersed with intrinsically disordered regions, often undergo liquid-liquid phase separation  
198 (LLPS), where molecules spontaneously demix from their solvent to form their own microscopic  
199 droplets (Banani et al., 2017; Forman-Kay et al., 2018; Holehouse and Pappu, 2018). The C-  
200 IDR of FMRP is capable of undergoing LLPS in isolation, in the context of full length, and in the  
201 presence of its cognate RNA substrates (Tsang et al., 2019). The multivalent interactions with  
202 diverging  $K_D$ s between various FMRP segments, R-loop substructures and R-loop resolving  
203 factors (*e.g.*, DHX9) can be the basis for the assembly of a phase-separated, membrane-less foci  
204 for resolving R-loops.

205

## 206 **ACKNOWLEDGEMENT**

207 We thank Drs. Leszek Kotula, Frank Middleton, Patricia Kane and Thidapi Wongsurawat for  
208 helpful discussions. We thank Dr. Helmut Pospiech and Late Dr. Frank Große from Leibniz  
209 Institute for Age Research - Fritz Lipmann Institute (FLI) at Jena, Germany for providing P.  
210 Sung with the pFastBac-His-DHX9 construct. We also thank Charlotte Logan for assisting in  
211 cloning of FMRP mutant constructs and Nathan McKean for helping with protein purification of  
212 FMRP. R-loop structures in Figure 2 and model in Figure 4 were created with BioRender.com.

213 This work was supported by the National Institute of Health 5R00GM08137805 and GM118799-  
214 01A1 grants to W.F., the Department of Defense CDMRP Discovery award W81XWH-15-1-  
215 0204 to W.F., the Department of Defense grant PC160083 to H.H., the National Institute of  
216 Health grant R35CA241801 to P.S. and the National Institute of Health Award R35GM138097  
217 to A.B..

218

## 219 **AUTHOR CONTRIBUTION**

220 A.C. and W.F. conceived the study. A.C. and H.H. performed and analyzed the immunostaining  
221 experiments. A.C. performed chromatin fractionation and IP experiments with guidance from  
222 W.F. L.D. and A.B. designed and performed protein purification for all full length FMRP,  
223 FMRPI304N and FMRP domains. L.G. and X.X. performed some preliminary EMSA assays.  
224 A.D. designed and performed EMSA assays, purified DHX9 and performed FMRP:DHX9  
225 interaction assay, with P.S. providing experimental guidance and suggestions. A.C., A.B. and  
226 W.F. wrote the manuscript with input from all authors.

227

## 228 **CONFLICT OF INTEREST**

229 The authors declare no conflict of interest in this study.

230

## 231 MATERIALS AND METHODS

232 **Cell line growth and drug treatment conditions.** Human EBV transformed lymphoblastoid  
233 cell line, GM06990, was grown in RPMI1640 (Corning cell gro), supplemented with GlutaMAX  
234 (GIBCO), 15% heat-inactivated FBS (Fetal Bovine Serum, Benchmark), 100 IU/mL penicillin  
235 and 100 µg/mL streptomycin (Corning cell gro) at 37°C with 5% CO<sub>2</sub>. Cells were treated, at a  
236 density of 0.4-0.5x10<sup>6</sup> cells/ml, with 0.03 µM, 0.3 µM, or 0.6 µM APH (A. G. Scientific),  
237 solvent (DMSO, 0.02%, same as the concentration in the APH-treated samples) only, or nothing,  
238 for 24 h before harvest.

239 **Co-immunoprecipitation (Co-IP).** Approximately 6-7x10<sup>6</sup> cells were used for each IP reaction.  
240 Cells were resuspended in 1 ml IP lysis buffer [25 mM Tris-HCl pH 7.5 / 150 mM NaCl / 1%  
241 NP-40 / 1 mM EDTA / 5% glycerol / Halt protease inhibitor cocktail (Thermo scientific) / Halt  
242 phosphatase inhibitor cocktail (Thermo scientific)] and incubated on ice for 1 h. Cell lysates  
243 were centrifuged at 10,000 rpm for 10 m. Protein concentration in the supernatant was  
244 determined using Pierce protein assay reagent (Thermo Scientific). 50 µl of Dynabeads protein  
245 G (Invitrogen) per reaction were incubated with 200 µl antibody binding buffer [1X PBS/ 0.02%  
246 Tween 20] and 5 µg of anti-FMRP (Biolegend), or anti-DHX9 (Santa Cruz Biotechnology), or  
247 IgG (Biolegend) in a rotator for 10 m at room temperature. The immuno-complex was rinsed  
248 with 200 µl antibody binding buffer at room temperature, followed by incubation with 500 µg of  
249 cell lysate per reaction at 4°C overnight. After incubation the supernatant was saved as flow-  
250 through (FT) and the beads were washed twice with IP lysis buffer without NP-40, saving each  
251 wash. 50 µl 2X Laemmli buffer was added to the beads and boiled for elution, before analysis  
252 on 8% SDS-PAGE gels and western blotting using anti-FMRP (Cell signaling, 1:500), anti-  
253 GAPDH (Thermo scientific, 1:4000) or anti-DHX9 (Santa Cruz Biotechnology, 1:500).

254 **Subcellular fractionation.** Cells were grown to a density of 0.4-0.5x10<sup>6</sup> cells/ml with >90%  
255 viability. Cells were treated for 24 h with aphidicolin, DMSO or nothing. Samples were  
256 collected as aliquots of approximately 5x10<sup>6</sup> cells, washed twice with PBS, then frozen for  
257 storage. Each thawed aliquot of cells was resuspended in 500 µl Farham's lysis buffer without  
258 NP-40 [5 mM PIPES pH 8.0 / 85 mM KCl / Halt protease inhibitor cocktail] and incubated on  
259 ice for 2 m. 50 µl of the cell lysate thus prepared was collected as a whole cell extract control  
260 and the remaining lysate was spun at 1300 g for 4 m to pellet nuclei. The supernatant served as  
261 the crude cytoplasmic fraction. The nuclear pellet was resuspended in 150 µl Farham's lysis  
262 buffer and incubated for 20-30 m at 4°C and served as the nuclear fraction. Equal volume of 2X  
263 Laemmli buffer were added and samples were boiled and later sonicated. Approximately 3x10<sup>5</sup>  
264 cell equivalent per fraction was used for electrophoresis on a 12% SDS-PAGE gel, followed by  
265 western analysis. Densitometry of autoradiogram was done using ImageJ  
266 (<https://imagej.nih.gov/ij/>) to calculate the percentages of FMRP in the nuclear and cytoplasmic  
267 fractions.

268 **Western blot.** Whole cell lysates were prepared in lysis buffer [50 mM Tris-HCl pH 7.5 / 0.5 M  
269 NaCl / 10 mM MgCl<sub>2</sub> / 1% NP-40 / Halt protease inhibitor cocktail / Halt phosphatase inhibitor  
270 cocktail] and at least 20 µg of proteins were analyzed by 10% SDS-PAGE before western  
271 blotting. The following antibodies were used: anti-FMRP (Biolegend, 1:1000), anti-Histone H3  
272 (Cell Signaling, 1:500) and anti-GAPDH (Thermo scientific, 1:2000).

273 **Immunocytochemistry and microscopy.** Approximately 3x10<sup>6</sup> cells having undergone drug  
274 treatment described above were washed twice in PBS before fixing with 500 µl 4%



275 paraformaldehyde in microfuge tubes. Cells were washed with 500  $\mu$ l 1X PBS twice, fixed with  
276 500  $\mu$ l 4% paraformaldehyde for 20 m at room temperature, followed by gently washing with 1X  
277 PBS three times. Cells were then blocked with 500  $\mu$ l PBSAT (1% BSA, 0.5% Triton X in 1X  
278 PBS), followed by incubation with 100  $\mu$ l of primary antibody solution for 1 h, washed with  
279 PBSAT, and incubation with 100  $\mu$ l secondary antibody for 1 h. Cells were then washed with  
280 PBSAT followed by PBS, and resuspended in mounting media (Prolong Diamond antifade plus  
281 DAPI, Invitrogen) before being placed as a drop onto microscope slides. Coverslips were  
282 carefully placed on top of the mounted drops and allowed to solidify for 24 h before imaging on  
283 Leica STP 800 wide-field fluorescence microscope (for lymphoblasts). Antibodies used for  
284 immunostaining include the following: primary antibodies (anti-FMRP, Cell signaling, 1:200 and  
285 S9.6, Kerafast, 1:500;) and secondary antibodies (Alex fluor 488, 568, and 647, Invitrogen,  
286 1:400). To determine localization of FMRP and R-loop in the nucleus, 3D image stacks were  
287 acquired from sixty-one 2D imaging planes with a step size of 0.11 micron using Metamorph.  
288 For images shown in Figure 1, a single Z-plane image at approximately the center of the stack  
289 was shown for each sample. DAPI was used to create a ROI which was overlaid and colored  
290 white to indicate nucleus. Images were adjusted for background and contrast and smoothed  
291 using a gaussian blur of 0.7 in Fiji.

292 **Cloning and protein purification.** As previously outlined in Tsang et al (Tsang et al., 2019)  
293 and briefly described here, codon optimized full length human FMRP Isoform 1 cDNA was  
294 generated by gene synthesis (GeneScript, Inc) and was subcloned into a pET-SUMO vector  
295 (Invitrogen). This pET-SUMO-FMRP plasmid was used as a template to generate (i) full length  
296 I304N mutant, (ii) FMRP-WT and FMRP-I304N mutant N-Folds (residues 1-455 without and  
297 with the I304N substitution, respectively), and (iii) C-IDR (residues 445-632) via QuikChange  
298 Site-Directed Mutagenesis (Agilent) for protein expression. The fidelity of these constructs was  
299 confirmed by Sanger sequencing (Eurofins Genomics, Louisville, KY). Each construct was  
300 transformed into *Escherichia coli* BL21(DE3) Codon Plus Cells (Agilent). Select colonies were  
301 inoculated in 50 ml of Luria Broth (LB) medium, before dilution into 1 L fresh LB medium in a  
302 Fernbach flask and grown at 37°C. Protein expression was induced with 1 mM isopropyl- $\beta$ -D-  
303 thiogalactopyranoside (IPTG) at an optical density (600 nm) of ~0.6 and was incubated at 16°C  
304 for 18 h. Cells were harvested by centrifugation at 15,000 rpm for 30 m. The supernatant was  
305 carefully discarded, and each cell pellet was stored at -20°C until ready for protein purification.

306 To begin purification, frozen cell pellets were thawed and re-suspended in 100 ml of lysis buffer  
307 containing 100 mM NaCl, 50 mM Na<sub>2</sub>PO<sub>4</sub>, 200 mM Arginine HCl, 200 mM Glutamic acid, 10%  
308 Glycerol, 10 mM  $\beta$ -mercaptoethanol, and 1% CHAPS, pH 7.4, supplemented with DNase I,  
309 lysozyme and protease inhibitors (bestatin, pepstatin, and leupeptin). Cells were lysed by  
310 sonication and the lysate was subjected to centrifugation at 15,000 rpm for 30 m. The  
311 supernatant was loaded onto a 20 ml HisTrap HP column (GE Healthcare) equilibrated in the  
312 binding buffer (i.e. same composition as lysis buffer, but without DNase I and lysozyme) and  
313 incubated at 4°C for 30 m. The column was extensively washed three times with 30 ml of the  
314 equilibration buffer. SUMO-fusion proteins were eluted using the same equilibration buffer  
315 supplemented with 500 mM imidazole, and fractions containing proteins were combined. A 6X-  
316 His-tagged Ulp protease was added to cleave the His-SUMO tag at room temperature overnight  
317 with rocking. Completion of the Ulp cleavage reaction was confirmed by SDS-PAGE. After  
318 cleavage, the protein solution was passed through a 0.2  $\mu$ m filter to remove any aggregated  
319 product, before it was concentrated using a 5 kDa-cutoff Amicon concentrator by centrifugation

320 at 4,000 rpm at room temperature. The concentrated protein solution is again filtered before  
321 being loaded onto an equilibrated Superdex 200 size exclusion column (GE Healthcare) to  
322 separate the FMRP constructs from the Ulp protease and the His-SUMO fusion tag. Fractions  
323 containing pure FMRP proteins were identified by SDS-PAGE and combined for storage at -  
324 80°C.

325 DHX9-His was expressed by transducing 800 ml Tni cell culture in ESF921 serum-free media  
326 (Expression Systems) at a density of  $1 \times 10^6$  cells/ml with 16 ml baculoviral suspension (generated  
327 in Sf9 cells) and grown for 70 h at 27°C with shaking. Cell pellet was resuspended in a lysis  
328 buffer containing 50 mM Tris-HCl, pH 7.5, 500 mM KCl, 10% glycerol, 1 mM EDTA, 1 mM  
329 DTT, 0.01% NP-40, 2 mM ATP, 4 mM MgCl<sub>2</sub>, 10 mM Imidazole, cOmplete protease inhibitor  
330 cocktail (MilliporeSigma), and 1mM PMSF, with sonication. The lysate was clarified by  
331 ultracentrifugation at 40,000 rpm for 45 m. The clarified lysate was incubated with 1 ml Ni-  
332 NTA resin (Qiagen) for 1 h, followed by washing the resin with 400 ml wash buffer-A  
333 containing 50 mM Tris-HCl, pH 7.5, 1000 mM KCl, 10% glycerol, 1 mM EDTA, 1 mM DTT,  
334 0.01% NP-40, 4 mM ATP, 8 mM MgCl<sub>2</sub> and 20 mM Imidazole. Protein-bound resin was  
335 washed again with 50 ml wash buffer-B containing 50 mM Tris-HCl, pH 7.5, 100 mM KCl, 10%  
336 glycerol, 1 mM EDTA, 1 mM DTT, 0.01% NP-40, and 20 mM Imidazole, followed by elution  
337 with 10 ml elution buffer containing 50 mM Tris-HCl, pH 7.5, 100 mM KCl, 10% glycerol, 1  
338 mM EDTA, 1 mM DTT, 0.01% NP-40, 300 mM Imidazole and cOmplete protease inhibitor  
339 cocktail (MilliporeSigma). The elution was subjected to ion exchange purification with  
340 equilibrated Hitrap SP HP (1ml) column at a gradient of 100-500 mM KCl. The peak fractions  
341 containing the protein were pooled together and purified again with HitrapQ (1 ml) column. The  
342 peak fraction was aliquoted, flash frozen with liquid nitrogen and stored at -80°C. The protein  
343 was also evaluated via size exclusion chromatography by loading 400 µl of the Hitrap SP HP  
344 purified fraction onto Superdex 200 increase 10/300 GL column (GE Healthcare), and a  
345 monodisperse peak was obtained at 11.8 ml elution fraction.

346 **Electrophoretic mobility shift assay (EMSA).** DNA or RNA was labelled at 5'-termini with  
347 T4-Polynucleotide kinase (NEB) using  $\gamma$ -P<sup>32</sup>-ATP as indicated in [Figure 2](#). The oligo sequences  
348 are listed in [Table S1](#). R-loops, RNA-DNA hybrids or duplex DNA substrates were generated  
349 by annealing the labelled oligonucleotide with the complementary cold oligonucleotides in  
350 equimolar ratio, as indicated in [Table S2](#), by gradually decreasing temperature from 95°C to 4°C.  
351 Prior to binding assays all the substrates were checked by electrophoresis in 5% native TAE  
352 (30 mM Tris-acetate, pH 7.4 and 0.5 mM EDTA) polyacrylamide gel.

353 *Binding assay.* 1 nM of R-loop, RNA-DNA hybrid, dsDNA, bubble DNA, ssDNA, or RNA  
354 substrate was mixed with 1 µl of protein at concentrations indicated in [Figure 2](#), in a buffer  
355 composed of 25 mM Tris-HCl (pH 7.5), 100 mM KCl, 5 µg/ml BSA, 5 mM EDTA, with a final  
356 volume of 10 µl. This mixture was incubated 30 m on ice, followed by addition of 10 µl loading  
357 buffer composed of 50% glycerol, 20 mM Tris-HCl, pH 7.4, 0.5 mM EDTA, 0.05% Orange G.

358 *Polyacrylamide gel electrophoresis.* Electrophoretic separation of the protein-bound substrates  
359 was carried out by running the mix in 5% native TAE gels, at 110V for 90 m at 4°C. The gels  
360 were vacuum dried for 30 m at 80°C on a gel dryer and exposed to phosphorimaging screen  
361 overnight. Imaging was done using Typhoon molecular imager (Amersham) and bands were  
362 quantified using ImageQuant TL 8.0 image analysis software.

363 ***In vitro* protein binding assay (for FMRP protein domains and DHX9-His).** 5 µg DHX9-His

364 was incubated with 10 $\mu$ l Ni-NTA beads in a binding buffer containing 50 mM Tris-HCl, pH 7.5,  
365 150 mM KCl, 10% glycerol, 1 mM EDTA, 1 mM DTT, 0.01% NP-40, 0.1% Tween-20, 10 mM  
366 Imidazole, and 1  $\mu$ l benzonase (MilliporeSigma) for 1 h, with mild shaking at 4°C. The  
367 supernatant was removed, and beads were washed three times with 200  $\mu$ l binding buffer. The  
368 binding buffer was completely removed and DHX9-His bound Ni-NTA were further incubated  
369 for 15 m with 5  $\mu$ g FMRP (full length)-WT, N-Fold-WT, N-Fold-I304N, or C-IDR (as indicated  
370 in the figures) in 20  $\mu$ l binding buffer. The protein bound resins were spun down and the  
371 supernatants were taken out carefully. 5  $\mu$ l loading buffer was added to supernatants. The resins  
372 in each tube was washed three times with 200  $\mu$ l wash buffer (same buffer with 20 mM  
373 Imidazole, and 200 mM KCl, without benzonase). The bound proteins were eluted with 25  $\mu$ l  
374 1X Laemmli buffer. Equal volume of supernatants and the pulldowns were analyzed in 4-15%  
375 polyacrylamide gradient gel.

376



## 377 **Figure Legends**

378

379 **Figure 1. FMRP is enriched in the nucleus upon replication stress.** (A) Subcellular  
380 fractionation of FMRP. Western blot showing, whole cell extract (W), cytoplasmic fraction (C)  
381 and nuclear fraction (N) of lymphoblastoid cells from unaffected control (NM) with and without  
382 replication stress. GAPDH and Histone H3 serve as cytoplasmic and nuclear controls,  
383 respectively. Two independent experiments were conducted, and one representative experiment  
384 is shown. (B) Quantification of FMRP, GAPDH and Histone H3 intensity shows increased  
385 percentage of FMRP in the nuclear fraction under APH stress. GAPDH shows minimum  
386 occupancy in the nucleus while Histone H3 shows maximum occupancy indicating the purity of  
387 fraction. Percentage of nuclear fraction of proteins expressed as the percentage of the band  
388 intensity for “N” over that of the sum of “N” and “C” for each condition. Error bars indicate  
389 standard error of mean in two independent experiments. One-way ANOVA followed by Tukey’s  
390 multiple comparison test. \*,  $p = 0.033$ . (C) Co-localization of FMRP and RNA:DNA hybrids.  
391 Immunofluorescence images of untreated, DMSO and APH treated NM cells co-stained for  
392 RNA:DNA hybrids (cyan), FMRP (magenta) and nucleus (yellow, outlined). Immuno-staining  
393 is shown in a single Z-plane. Scale bar, 5  $\mu\text{m}$ .

394

395 **Figure 2. FMRP directly binds R-loops *in vitro*.** (A) Schematic representation of FMRP  
396 protein domains, indicating the fold region and the C-terminus intrinsically disordered region (C-  
397 IDR). The folded FMRP domain also harbor the isoleucine to asparagine mutation at residue  
398 304 which causes FXS. (B) Nucleic acid structures used in the electrophoretic mobility shift  
399 assay (EMSA) to determine binding interaction with FMRP N-Fold domain or FMRP C-IDR.  
400 Blue strand represents DNA and red represents RNA, while asterisk indicates  $P^{32}$  label at the 5’-  
401 end of the DNA or RNA strand. a- R-loop with 5’-RNA overhang (5’-RNA ovh), b- R-loop with  
402 no overhang (no ovh), c- Bubble DNA (90 bp), d- RNA:DNA hybrid (no ovh), e- RNA:DNA  
403 hybrid (5’-RNA ovh), f- Single-stranded DNA (ssDNA), g- Double-stranded DNA (dsDNA) and  
404 h- RNA (30 or 60 bs). (C&D) Representative EMSAs for interaction between R-loop with 5’-  
405 RNA ovh and the N-Fold and C-IDR domains. Sub., substrates. (E) Representative EMSA for  
406 interaction between R-loop without ovh and the C-IDR. (F-H) Quantification of the percentage  
407 of bound nucleic acid substrates at the indicated protein concentrations for N-Fold-WT (F), N-  
408 Fold-I304N (G) and C-IDR (H). (I) Representative EMSA for interaction between R-loop with  
409 5’- RNA ovh and the full length FMRP with or without I304N mutation. (J) Quantification of  
410 the percentage of bound nucleic acid substrates at the indicated protein concentrations for  
411 FMRP-WT. Note, FMRP-I304N showed nearly identical binding to all nucleic acids except for  
412 R-loop (no ovh) and RNA (60 bs). See Figure 2-figure supplements 2&3 for details. The free  
413 and bound substrates labeled for (C) is true for all EMSA gels.

414

415 **Figure 3. FMRP directly interacts with R-loop resolving factor DHX9.** (A) Purification of  
416 Histidine-tagged DHX9 recombinant protein (DHX9-His). (B-D) *In vitro* protein binding assays  
417 for DHX9-His and full length FMRP (B), FMRP domains (C) and N-Fold-WT or N-Fold-I304N  
418 (D). (E) Co-immunoprecipitation of FMRP by immunoprecipitating with anti-FXR1 monoclonal  
419 antibody and immunoblotted for FMRP and FXR1. GAPDH served as negative control. (F) Co-  
420 immunoprecipitation of FMRP by immunoprecipitating with anti-DHX9 monoclonal antibody

421 and immunoblotted for FMRP, DHX9 and TOP III $\beta$ . GAPDH served as negative control. The  
422 black asterisks indicate the lower band of a doublet signal in the “IP-DHX9” lane is the DHX9  
423 protein, which is accumulated in the immunoprecipitated complex and absent in the IgG-  
424 precipitated control complex (“IP-IgG” lanes).

425

426 **Figure 4. Proposed mechanism of R-loop resolution by FMRP and DHX9.** We hypothesize  
427 that FMRP interacts with R-loops, which form as a result of transcription-replication conflict (T-  
428 R), through complex arrangement(s) of its N-terminal Fold (N-Fold) domain and C-IDR. We  
429 propose that i) the C-IDR directly binds R-loop through the recognition of the triple-stranded  
430 structure, probably at the 3'-end in normal cells and the KH domains of N-Fold binds either the  
431 displaced ssDNA (not depicted) or the trailing RNA overhang (depicted), ii) the Agetet domain  
432 of N-Fold binds R-loop resolving factors, such as DHX9, probably through the C-terminus RGG  
433 domain of DHX9 containing methylated arginine residues (“Me”). The isoleucine residue in the  
434 KH2 domain (“I304”) is important for these interactions. The I304N mutation abolishes the  
435 binding to ssDNA, RNA, and DHX9. Through bridging the interactions between nucleic acids  
436 and proteins by multivalent interactions, FMRP recruits R-loop resolving factors to the R-loops  
437 (iii), allowing replication to proceed normally (iv). In the absence of FMRP, stabilized R-loops  
438 suffer from strand breakage, likely in the displaced ssDNA, and result in DSB formation at gene  
439 loci involved in neurodevelopment pathways and in transcription factors.

440

441

## 442 **References**

- 443 Banani, S.F., Lee, H.O., Hyman, A.A., and Rosen, M.K. (2017). Biomolecular condensates:  
444 organizers of cellular biochemistry. *Nat Rev Mol Cell Biol* 18, 285-298.
- 445 Banerjee, A., Ifrim, M.F., Valdez, A.N., Raj, N., and Bassell, G.J. (2018). Aberrant RNA  
446 translation in fragile X syndrome: From FMRP mechanisms to emerging therapeutic strategies.  
447 *Brain Res* 1693, 24-36.
- 448 Bechara, E.G., Didiot, M.C., Melko, M., Davidovic, L., Bensaid, M., Martin, P., Castets, M.,  
449 Pognonec, P., Khandjian, E.W., Moine, H., *et al.* (2009). A novel function for fragile X mental  
450 retardation protein in translational activation. *PLoS Biol* 7, e16.
- 451 Chakraborty, A., Jenjaroenpun, P., Li, J., El Hilali, S., McCulley, A., Haarer, B., Hoffman, E.A.,  
452 Belak, A., Thorland, A., Hehnly, H., *et al.* (2020). Replication Stress Induces Global  
453 Chromosome Breakage in the Fragile X Genome. *Cell Rep* 32, 108179.
- 454 Chakraborty, P., and Grosse, F. (2011). Human DHX9 helicase preferentially unwinds RNA-  
455 containing displacement loops (R-loops) and G-quadruplexes. *DNA Repair (Amst)* 10, 654-665.
- 456 Ciaccio, C., Fontana, L., Milani, D., Tabano, S., Miozzo, M., and Esposito, S. (2017). Fragile X  
457 syndrome: a review of clinical and molecular diagnoses. *Ital J Pediatr* 43, 39.
- 458 Cristini, A., Groh, M., Kristiansen, M.S., and Gromak, N. (2018). RNA/DNA Hybrid  
459 Interactome Identifies DXH9 as a Molecular Player in Transcriptional Termination and R-Loop-  
460 Associated DNA Damage. *Cell Rep* 23, 1891-1905.
- 461 De Boulle, K., Verkerk, A.J., Reyniers, E., Vits, L., Hendrickx, J., Van Roy, B., Van den Bos, F.,  
462 de Graaff, E., Oostra, B.A., and Willems, P.J. (1993). A point mutation in the FMR-1 gene  
463 associated with fragile X mental retardation. *Nature genetics* 3, 31-35.
- 464 De Magis, A., Manzo, S.G., Russo, M., Marinello, J., Morigi, R., Sordet, O., and Capranico, G.  
465 (2019). DNA damage and genome instability by G-quadruplex ligands are mediated by R loops  
466 in human cancer cells. *Proc Natl Acad Sci U S A* 116, 816-825.
- 467 Dockendorff, T.C., and Labrador, M. (2019). The Fragile X Protein and Genome Function. *Mol*  
468 *Neurobiol* 56, 711-721.
- 469 Dominguez-Sanchez, M.S., Barroso, S., Gomez-Gonzalez, B., Luna, R., and Aguilera, A. (2011).  
470 Genome instability and transcription elongation impairment in human cells depleted of  
471 THO/TREX. *PLoS genetics* 7, e1002386.
- 472 Feng, Y., Absher, D., Eberhart, D.E., Brown, V., Malter, H.E., and Warren, S.T. (1997a). FMRP  
473 associates with polyribosomes as an mRNP, and the I304N mutation of severe fragile X  
474 syndrome abolishes this association. *Molecular cell* 1, 109-118.
- 475 Feng, Y., Gutekunst, C.A., Eberhart, D.E., Yi, H., Warren, S.T., and Hersch, S.M. (1997b).  
476 Fragile X mental retardation protein: nucleocytoplasmic shuttling and association with

- 477 somatodendritic ribosomes. *The Journal of neuroscience : the official journal of the Society for*  
478 *Neuroscience* 17, 1539-1547.
- 479 Forman-Kay, J.D., Kriwacki, R.W., and Seydoux, G. (2018). Phase Separation in Biology and  
480 Disease. *Journal of molecular biology* 430, 4603-4606.
- 481 Hein, M.Y., Hubner, N.C., Poser, I., Cox, J., Nagaraj, N., Toyoda, Y., Gak, I.A., Weisswange, I.,  
482 Mansfeld, J., Buchholz, F., *et al.* (2015). A human interactome in three quantitative dimensions  
483 organized by stoichiometries and abundances. *Cell* 163, 712-723.
- 484 Holehouse, A.S., and Pappu, R.V. (2018). Functional Implications of Intracellular Phase  
485 Transitions. *Biochemistry* 57, 2415-2423.
- 486 Lee, C.Y., McNerney, C., Ma, K., Zhao, W., Wang, A., and Myong, S. (2020). R-loop induced  
487 G-quadruplex in non-template promotes transcription by successive R-loop formation. *Nature*  
488 *communications* 11, 3392.
- 489 Mitrea, D.M., and Kriwacki, R.W. (2016). Phase separation in biology; functional organization  
490 of a higher order. *Cell Commun Signal* 14, 1.
- 491 Santoro, M.R., Bray, S.M., and Warren, S.T. (2012). Molecular mechanisms of fragile X  
492 syndrome: a twenty-year perspective. *Annu Rev Pathol* 7, 219-245.
- 493 Sitzmann, A.F., Hagelstrom, R.T., Tassone, F., Hagerman, R.J., and Butler, M.G. (2018). Rare  
494 FMR1 gene mutations causing fragile X syndrome: A review. *Am J Med Genet A* 176, 11-18.
- 495 Sjekloca, L., Konarev, P.V., Eccleston, J., Taylor, I.A., Svergun, D.I., and Pastore, A. (2009). A  
496 study of the ultrastructure of fragile-X-related proteins. *Biochem J* 419, 347-357.
- 497 Sjekloca, L., Pauwels, K., and Pastore, A. (2011). On the aggregation properties of FMRP--a link  
498 with the FXTAS syndrome? *The FEBS journal* 278, 1912-1921.
- 499 Sudhakaran, I.P., Hillebrand, J., Dervan, A., Das, S., Holohan, E.E., Hulsmeier, J., Sarov, M.,  
500 Parker, R., VijayRaghavan, K., and Ramaswami, M. (2014). FMRP and Ataxin-2 function  
501 together in long-term olfactory habituation and neuronal translational control. *Proc Natl Acad*  
502 *Sci U S A* 111, E99-E108.
- 503 Tsang, B., Arsenault, J., Vernon, R.M., Lin, H., Sonenberg, N., Wang, L.Y., Bah, A., and  
504 Forman-Kay, J.D. (2019). Phosphoregulated FMRP phase separation models activity-dependent  
505 translation through bidirectional control of mRNA granule formation. *Proc Natl Acad Sci U S A*  
506 116, 4218-4227.
- 507 Vasilyev, N., Polonskaia, A., Darnell, J.C., Darnell, R.B., Patel, D.J., and Serganov, A. (2015).  
508 Crystal structure reveals specific recognition of a G-quadruplex RNA by a beta-turn in the RGG  
509 motif of FMRP. *Proc Natl Acad Sci U S A* 112, E5391-5400.

- 510 Yang, Y., McBride, K.M., Hensley, S., Lu, Y., Chedin, F., and Bedford, M.T. (2014). Arginine  
511 methylation facilitates the recruitment of TOP3B to chromatin to prevent R loop accumulation.  
512 *Molecular cell* 53, 484-497.
- 513 Zang, J.B., Nosyreva, E.D., Spencer, C.M., Volk, L.J., Musunuru, K., Zhong, R., Stone, E.F.,  
514 Yuva-Paylor, L.A., Huber, K.M., Paylor, R., *et al.* (2009). A mouse model of the human Fragile  
515 X syndrome I304N mutation. *PLoS genetics* 5, e1000758.
- 516 Zhang, T., Wallis, M., Petrovic, V., Challis, J., Kalitsis, P., and Hudson, D.F. (2019). Loss of  
517 TOP3B leads to increased R-loop formation and genome instability. *Open Biol* 9, 190222.
- 518 Zhou, L.T., Ye, S.H., Yang, H.X., Zhou, Y.T., Zhao, Q.H., Sun, W.W., Gao, M.M., Yi, Y.H.,  
519 and Long, Y.S. (2017). A novel role of fragile X mental retardation protein in pre-mRNA  
520 alternative splicing through RNA-binding protein 14. *Neuroscience* 349, 64-75.  
521  
522

523 **SUPPLEMENTARY INFORMATION**

524 **FIGURE SUPPLEMENTS**

525

526 **Figure 1-figure supplement 1.** (A) Total FMRP level expressed as ratio of FMRP over  
527 GAPDH in the whole cell extracts (n=2) from Figure 1A remained nearly constant in all  
528 conditions. (B) Volumetric 3D reconstruction in MetaMorph of an APH-treated normal cell.  
529 Montage representation of 360° rotation of the cell along the X-axis, FMRP in green, S9.6 in red,  
530 yellow indicates merge and points of co-localization when rotated vertically along the X-axis.  
531 Numbers indicate the angle of rotation. (C) Cartoon illustration of a cell with a nucleus (blue) in  
532 3D indicating rotation along the X-axis. (D) Video attachment of the same cell in Figure 1-  
533 figure supplement 1-source data 1.

534

535 **Figure 2—figure supplement 1. Purification of FMRP fragments, their interactions with**  
536 **various nucleic acid structures and purification of DHX9.** (A-C) Purification of FMRP  
537 protein domains for EMSA. The fusion proteins containing HIS-SUMO-tagged FMRP fragments  
538 were subject to Ulp cleavage to remove the tag, followed by FPLC to remove the cleaved HIS-  
539 SUMO as well as Ulp itself, as shown for N-Fold-WT (A). The same procedures were applied to  
540 the purification of N-Fold-I304N (B) and C-IDR (C). (D) Purification of full length FMRP-WT  
541 and FMRP-I304N.

542

543 **Figure 2—figure supplement 2.** Binding affinity of the FMRP fragments for the nucleic acid  
544 substrates were calculated as dissociation constants ( $K_{DS}$  in nM) averaged from two independent  
545 EMSA experiments.

546

547 **Figure 2—figure supplement 3.** Representative EMSA for all proteins and nucleic acids. #  
548 denotes that SDS/PK was not added in this sample.

549

550

551

552

553 **Table S1.** List of all oligonucleotides for making substrates for EMSA experiments.

554

Name	Size	Sequence
D1	90 nt	5'- CATTGCATATTTAAAACATGTTGGATCCCACGTTGCATGCTGATAGCCTACTAGAGCTG TATGAATTCAAATGACCTCTTATCAAGTGAC -3'
D2	90 nt	5'- GTCACCTTGATAAGAGGTCATTTGAATTCATGGCTTAGAGCTTAATTGCTGAATCTGGTG CTGGGATCCAACATGTTTTAAATATGCAATG-3'
D3	30 nt	5'- GGCTTAGAGCTTAATTGCTGAATCTGGTGC-3'
D4	60 nt	5'- ACGCTGCCGAATTCTACCAGTGCCTTGCTAGGACATCTTTGCCACCTGCAGGTTCCACC C -3'
D5	30 nt	5'- GGGTGAACCTGCAGGTGGGCAAAGATGTCCCAGCAAGGCACTGGTAGAATTCGGCAGC GT -3'
R1	60 nt	5'- GUGCUACGAUGCUAGUCGUAGCUCGGGAGUGCACCAGAUUCAGCAAUUAAGCUCUA AGCC- 3'
R2	30 nt	5'-GCACCAGAUUCAGCAAUUAAGCUCUAAGCC -3'

555

556 “nt”, nucleotide.



557 **Table S2.** Scheme for generating substrates for EMSA experiments.

558

R-loop with 5'-RNA overhang	D1+D2+R1
R-loop with no-RNA overhang	D1+D2+R2
RNA-DNA hybrid with 5'-RNA overhang	D3+R1
RNA-DNA hybrid with no RNA overhang	D3+R2
dsDNA	D4+D5
Bubble DNA	D1+D2
ssDNA	D1
RNA (60 nt)	R1
RNA (30 nt)	R2

559

560

# Figure 1

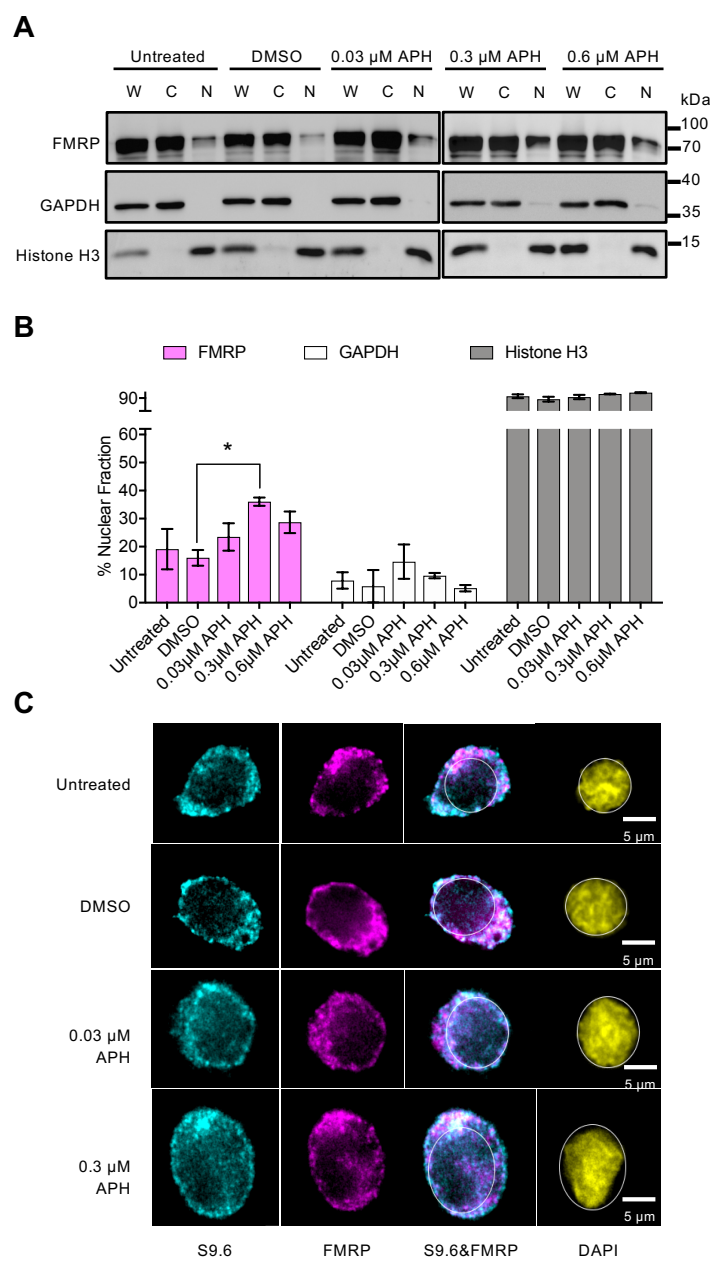


## Figure 2

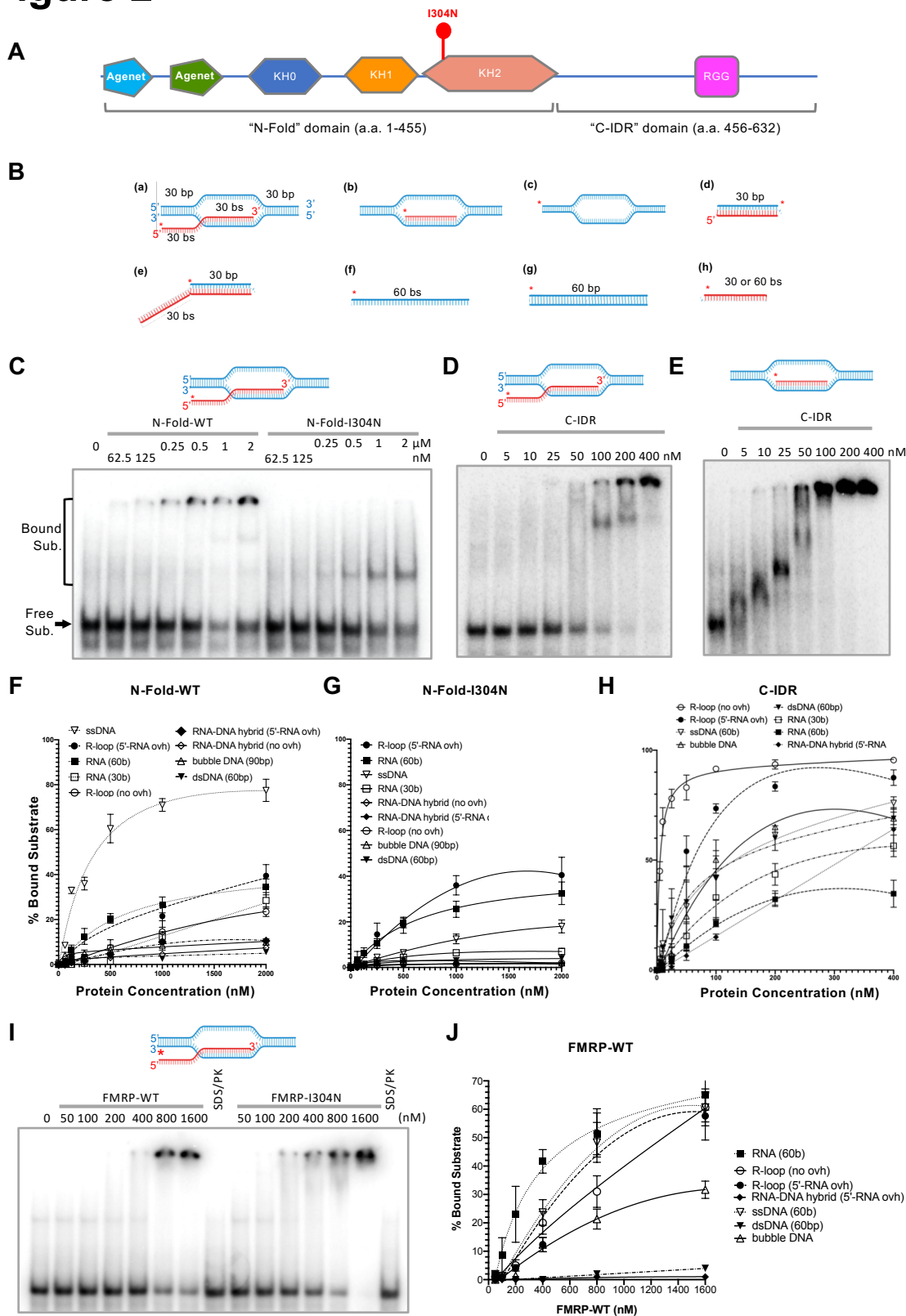


## Figure 3

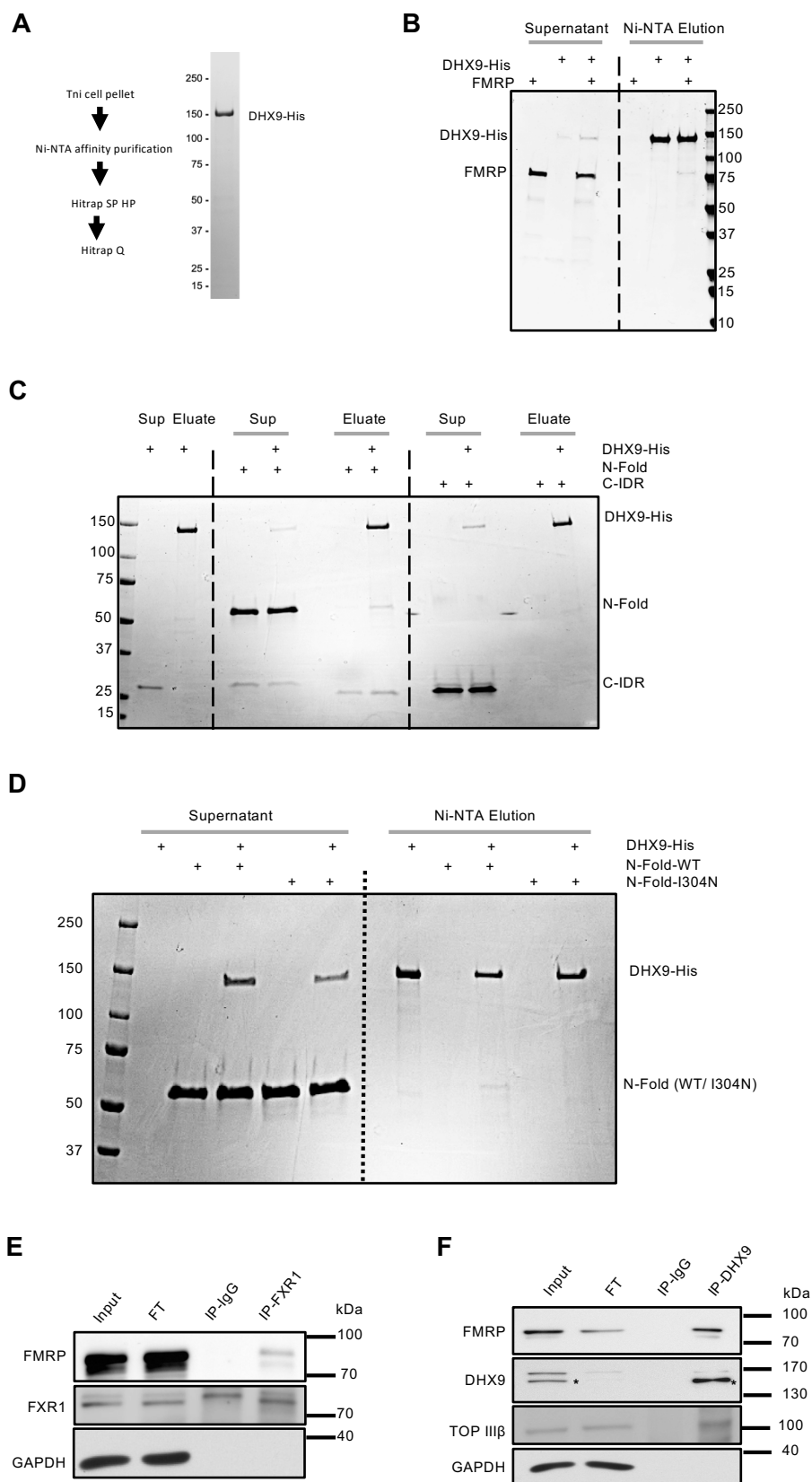


## Figure 4

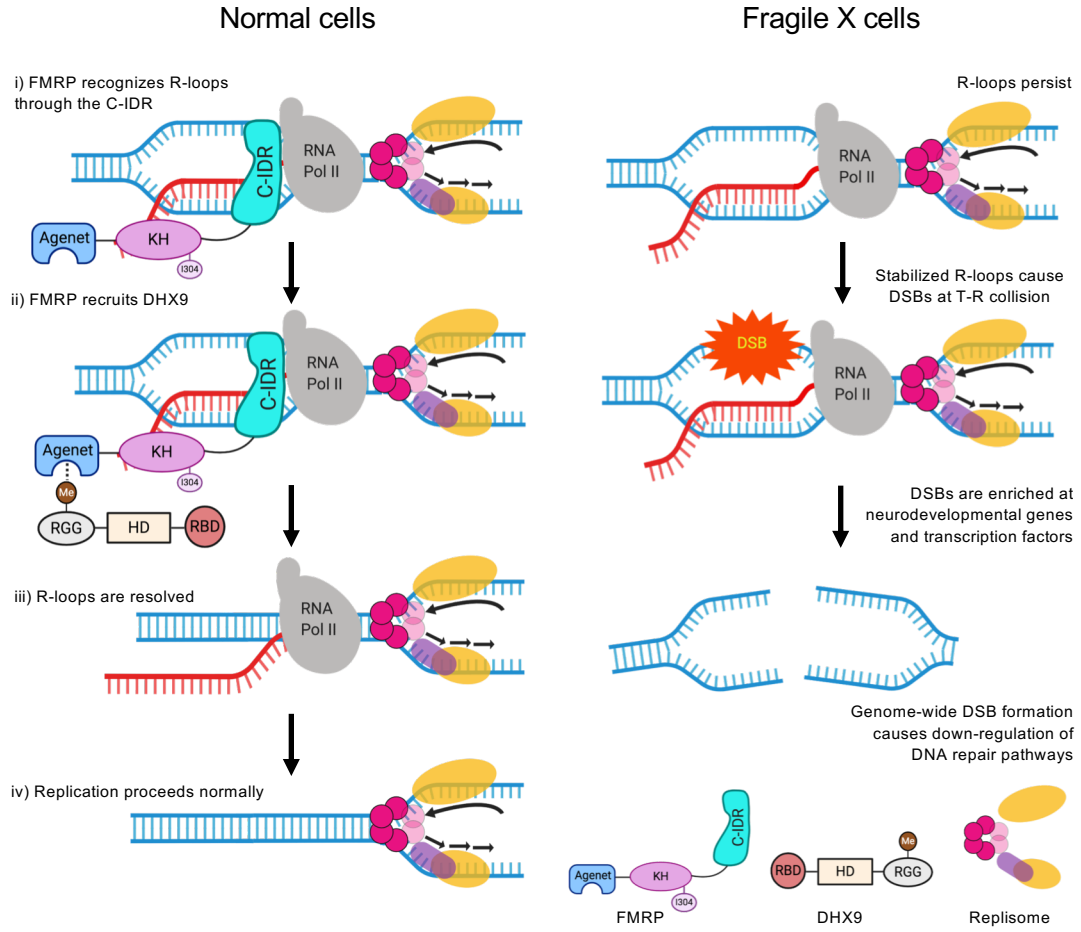


## Figure 1—figure supplement 1

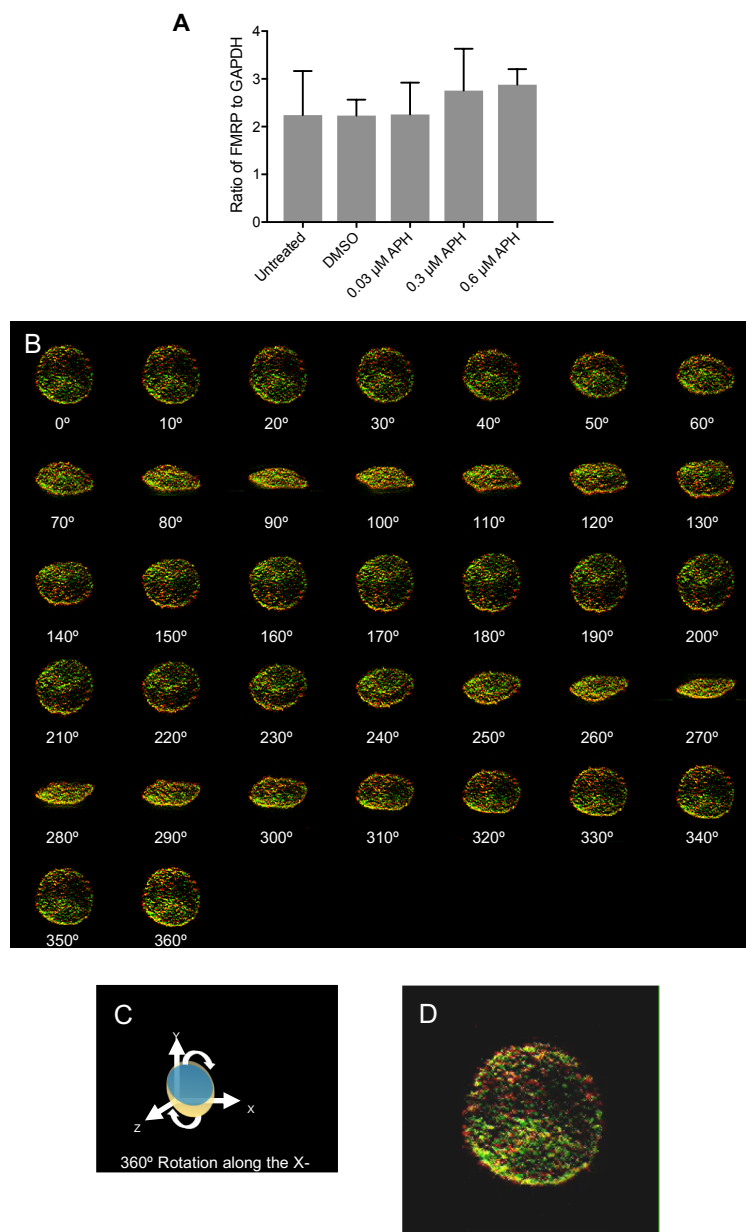


**Figure 1—figure supplement 1. (A)** Total FMRP level expressed as ratio of FMRP over GAPDH in the whole cell extracts ( $n=2$ ) from Figure 1A remained nearly constant in all conditions. **(B)** Volumetric 3D reconstruction in MetaMorph of an APH-treated normal cell. Montage representation of 360° rotation of the cell along the X-axis, FMRP in green, S9.6 in red, yellow indicates merge and points of co-localization when rotated vertically along the X-axis. Numbers indicate the angle of rotation. **(C)** Cartoon illustration of a cell with a nucleus (blue) in 3D indicating rotation along the X-axis. **(D)** Video attachment of the same cell in Figure 1—figure supplement 1—source data 1.

## Figure 2—figure supplement 1

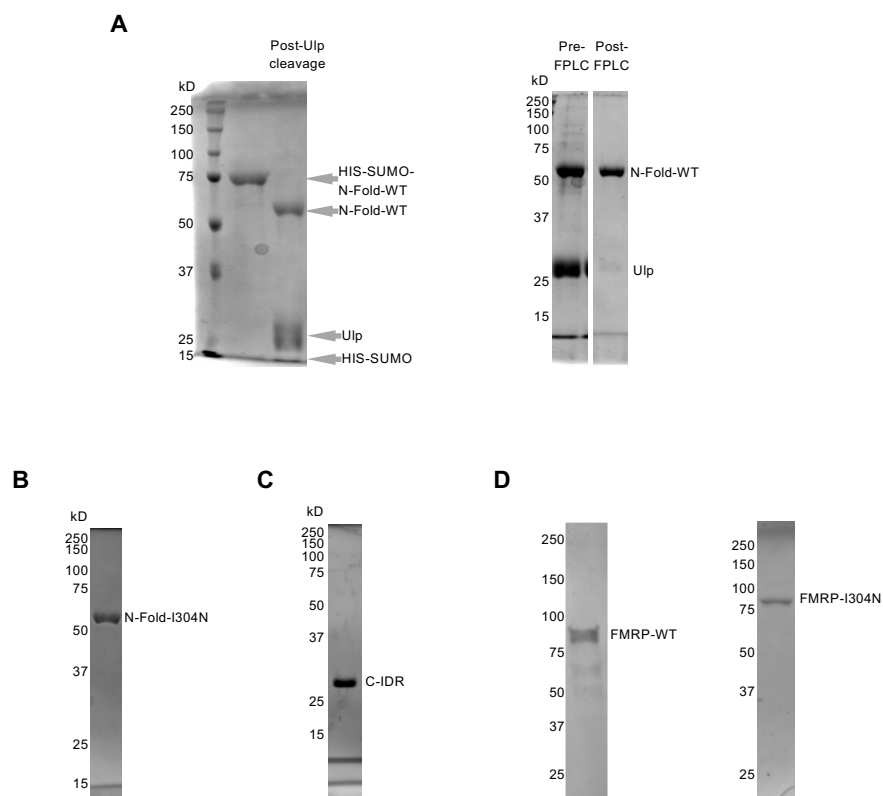


**Figure 2—figure supplement 1. Purification of FRMP fragments, their interactions with various nucleic acid structures and purification of DHX9. (A-C)** Purification of FMRP protein domains for EMSA. The fusion proteins containing HIS-SUMO-tagged FMRP fragments were subject to Ulp cleavage to remove the tag, followed by FPLC to remove the cleaved HIS-SUMO as well as Ulp itself, as shown for N-Fold-WT (A). The same procedures were applied to the purification of N-Fold-I304N (B) and C-IDR (C). (D) Purification of full length FMRP-WT and FMRP-I304N.



## Figure 2—figure supplement 2

**K<sub>D</sub> of FMRP domains for nucleic acid substrates**

Substrate	FMRP-WT	FMRP-I304N*	N-Fold-WT	N-Fold-I304N	C-IDR
R-loop (no ovh)	288.7 ± 4	213.7 ± 4.7	NA	NA	4.7 ± 3.9
R-loop (5' ovh)	NA	NA	322 ± 3.9	NA	149.1 ± 9.9
DNA bubble	NA	NA	NA	NA	NA
dsDNA (60 bp)	NA	NA	NA	NA	56.8 ± 7.1
RNA (30 bs)	NA	NA	NA	NA	360.2 ± 4.7
RNA (60 bs)	113.6 ± 6	311.6 ± 3.7	615.9 ± 2.2	NA	NA
ssDNA (60 bs)	NA	NA	380.9 ± 5.7	NA	79.6 ± 9.3
RNA-DNA hybrid	NA	NA	NA	NA	NA

**Figure 2—figure supplement 2.** Binding affinity of the FMRP fragments for the nucleic acid substrates were calculated as dissociation constants (K<sub>D</sub>s in nM) from EMSA experiments in Figure 2.

## Figure 2—figure supplement 3

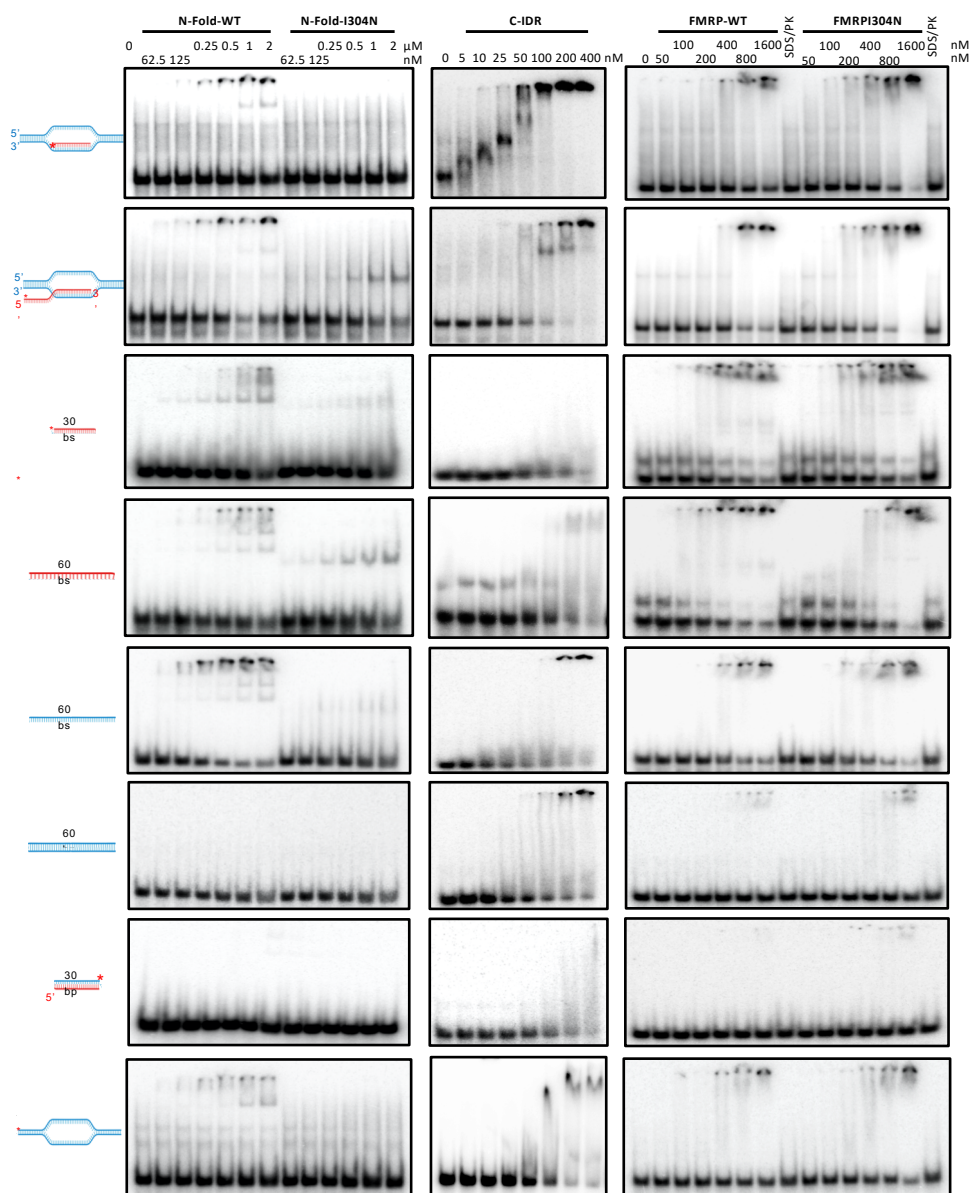


**Figure 2—figure supplement 3.** Representative EMSA for all proteins and nucleic acids.

## Figure 1—figure supplement 1

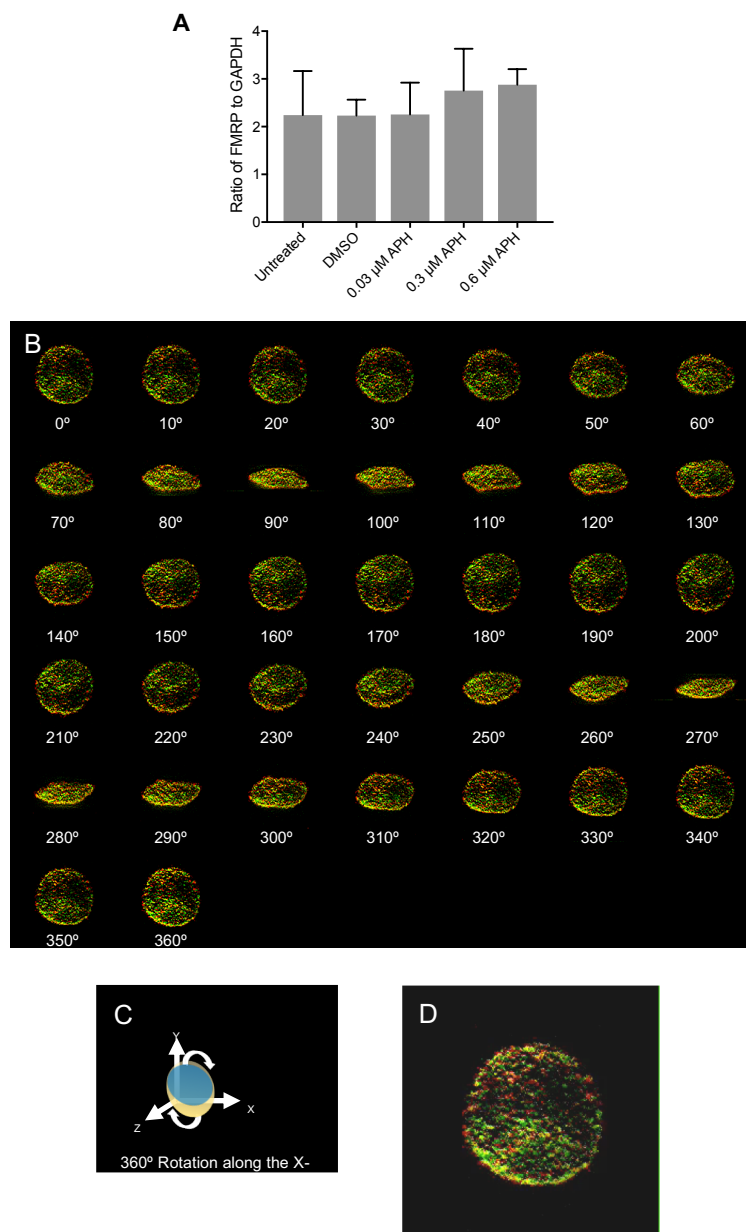


**Figure 1—figure supplement 1. (A)** Total FMRP level expressed as ratio of FMRP over GAPDH in the whole cell extracts ( $n=2$ ) from Figure 1A remained nearly constant in all conditions. **(B)** Volumetric 3D reconstruction in MetaMorph of an APH-treated normal cell. Montage representation of 360° rotation of the cell along the X-axis, FMRP in green, S9.6 in red, yellow indicates merge and points of co-localization when rotated vertically along the X-axis. Numbers indicate the angle of rotation. **(C)** Cartoon illustration of a cell with a nucleus (blue) in 3D indicating rotation along the X-axis. **(D)** Video attachment of the same cell in Figure 1—figure supplement 1—source data 1.

## Figure 2

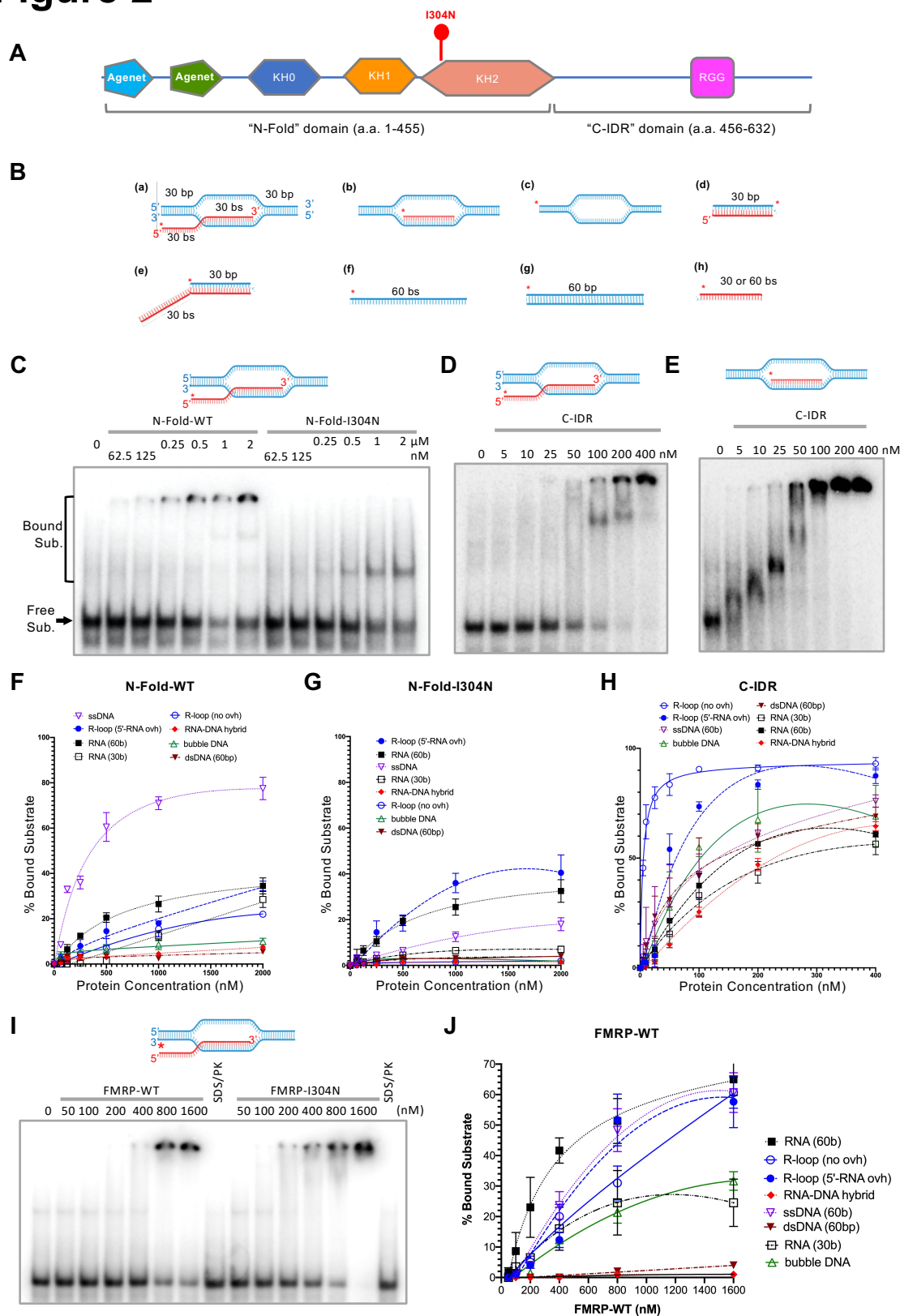


## Figure 2—figure supplement 1

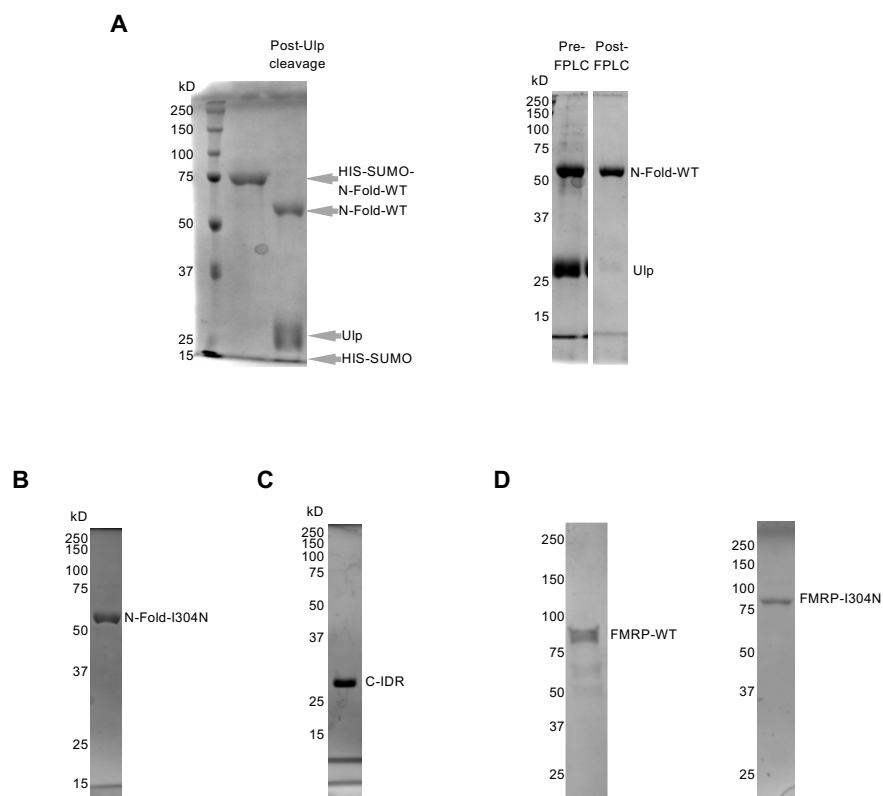


**Figure 2—figure supplement 1. Purification of FRMP fragments, their interactions with various nucleic acid structures and purification of DHX9. (A-C)** Purification of FMRP protein domains for EMSA. The fusion proteins containing HIS-SUMO-tagged FMRP fragments were subject to Ulp cleavage to remove the tag, followed by FPLC to remove the cleaved HIS-SUMO as well as Ulp itself, as shown for N-Fold-WT (A). The same procedures were applied to the purification of N-Fold-I304N (B) and C-IDR (C). (D) Purification of full length FMRP-WT and FMRP-I304N.

## Figure 2—figure supplement 2

**K<sub>D</sub> of FMRP domains for nucleic acid substrates**

Substrate	FMRP-WT	FMRP-I304N*	N-Fold-WT	N-Fold-I304N	C-IDR
R-loop (no ovh)	288.7 ± 4	213.7 ± 4.7	NA	NA	4.7 ± 3.9
R-loop (5' ovh)	NA	NA	322 ± 3.9	NA	149.1 ± 9.9
DNA bubble	NA	NA	NA	NA	NA
dsDNA (60 bp)	NA	NA	NA	NA	56.8 ± 7.1
RNA (30 bs)	NA	NA	NA	NA	360.2 ± 4.7
RNA (60 bs)	113.6 ± 6	311.6 ± 3.7	615.9 ± 2.2	NA	NA
ssDNA (60 bs)	NA	NA	380.9 ± 5.7	NA	79.6 ± 9.3
RNA-DNA hybrid	NA	NA	NA	NA	NA

**Figure 2—figure supplement 2.** Binding affinity of the FMRP fragments for the nucleic acid substrates were calculated as dissociation constants (K<sub>D</sub>s in nM) averaged from at least three EMSA experiments in Figure 2.

## Figure 2—figure supplement 3

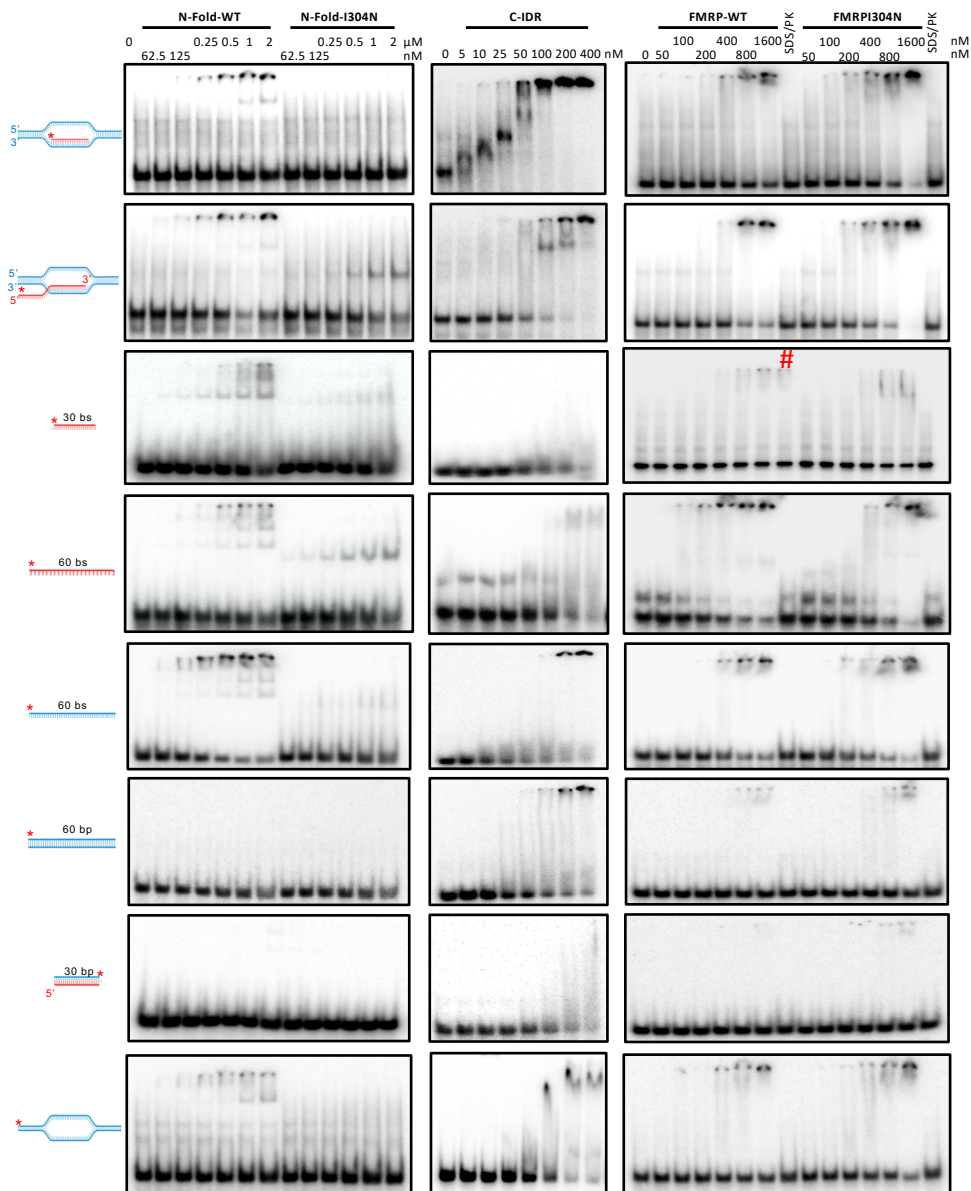


**Figure 2—figure supplement 3.** Representative EMSA for all proteins and nucleic acids. # denotes that SDS/PK was not added in this sample.



## Figure 3

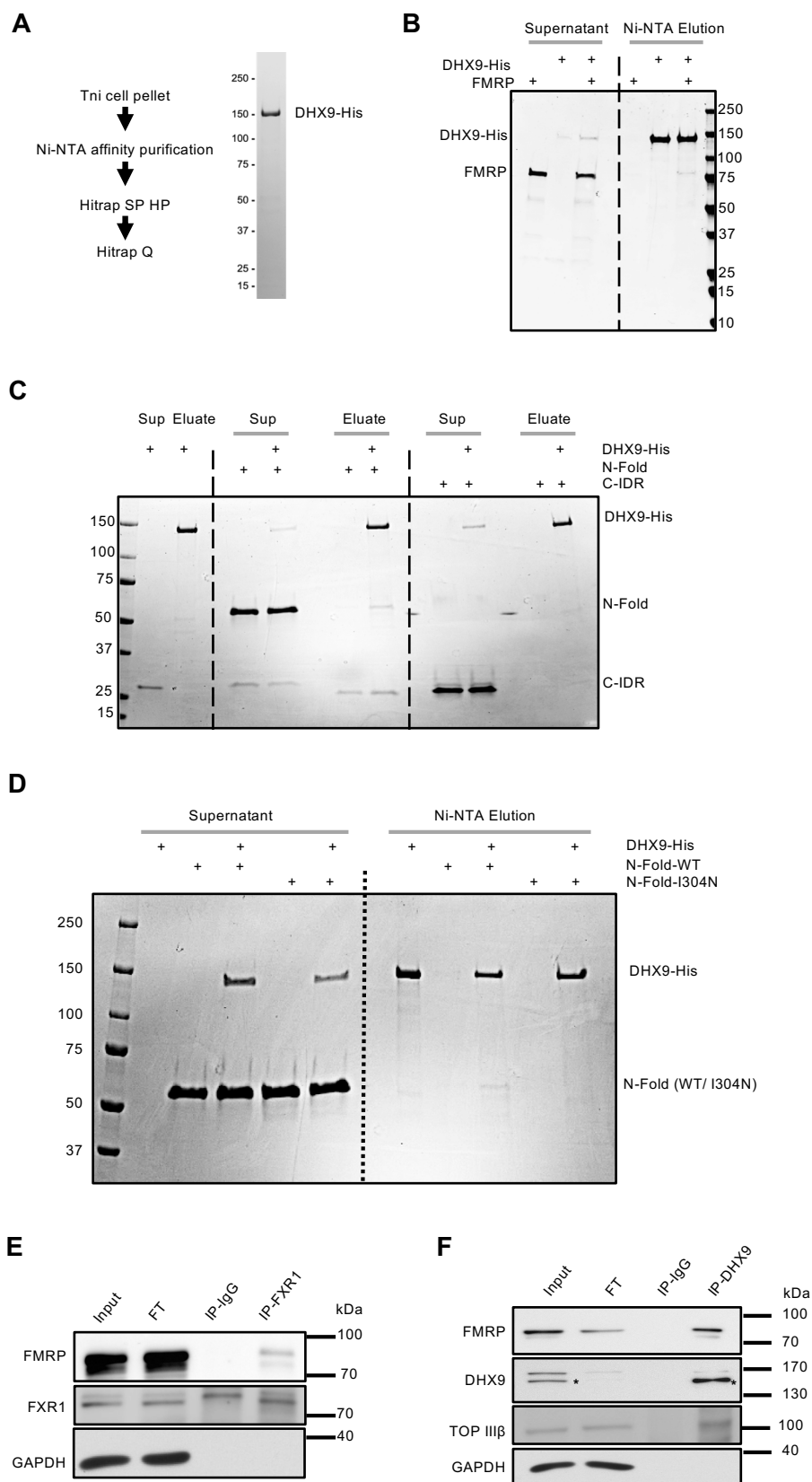


## Figure 4

